Journal of Molecular Graphics and Modelling 57 (2015) 131–142

Contents lists available at ScienceDirect

Journal of Molecular Graphics and Modelling

journal homepage: www.elsevier.com/locate/JMGM

Human PD-1 binds differently to its human ligands: A comprehensive modeling study

Clement Viricel[a,b], Marawan Ahmed[a], Khaled Barakat[a,c,d,*]

[a] Faculty of Pharmacy and Pharmaceutical Sciences, University of Alberta, Edmonton, AB, Canada
[b] Department of Mathematics, University of Claude Bernard Lyon 1, Lyon, France
[c] Li Ka Shing Institute of Virology, University of Alberta, Edmonton, Alberta, Canada
[d] Li Ka Shing Applied Virology Institute, University of Alberta, Edmonton, Alberta, Canada

ARTICLE INFO

Article history:
Accepted 31 January 2015
Available online 14 February 2015

Keywords:
PD1
PD-L1
PD-L2
Protein–Protein docking
ZDOCK
Molecular dynamics simulations

ABSTRACT

Programmed death-1 (PD-1) is a potent inhibitory receptor of T cells which binds to two different ligands, namely PD-L1 and PD-L2, and upon binding, it inhibits T cell activation, differentiation, and proliferation, leading to a state of immune tolerance. Blocking these interactions recently emerged as a 'game changer' approach in immunotherapy. Despite the significant therapeutic potential of targeting the PD-1 pathway, the interaction between human PD-1 and its two human ligands is not fully understood. Current crystal structures describe the interactions of mouse PD-1 with human PD-L1 or mouse PD-L2. However, recent mutational and nuclear magnetic resonance (NMR) analyses suggest that human PD-1 binds its human ligands differently compared to their mouse counterparts. No detailed model is currently available to consistently fit these data. The lack of these accurate structures constitutes a high barrier against rationally developing more effective and safer agents targeting these interactions. Here we describe for the first time two accurate models for human PD-1 bound to its two human ligands. Our methodology involved combining molecular dynamics (MD) simulations with protein–protein docking and binding energy analysis to predict the most probable binding conformations for PD1 to its ligands. Our results confirm the available experimental NMR and mutational data and reveal the most accurate atomistic details so far of how human PD-1 binds to human PD-Ls and why the two ligands bind with different affinities to the same receptor.

© 2015 Elsevier Inc. All rights reserved.

1. Introduction

T lymphocytes (T cells) preserve the immunological balance between self-tolerance and defending against microbes and cancer [1–3]. Leaping between the two extremes requires an intricate network of protein–protein interactions that can either inhibit T cells-mediated immune responses targeted against self-tissues or stimulate them to defend against invading pathogens [4]. Tumors and infectious diseases can hide from the immune system by hijacking those inhibitory pathways to attenuate T cells' signaling, leading to a state of immune tolerance. Blocking these immune inhibitory checkpoints recently emerged as a 'game changer' approach in cancer immunotherapy. Among these pathways is the Cytotoxic T Lymphocyte Antigen-4 (CTLA-4) pathway and more recently the programmed death-1 (PD-1) pathway, for which antibodies directed toward PD1 have been selected as drug of the year for 2013 [1,2,5]. These agents possess a unique mode of action; they restore exhausted T cells' functions and reactivate the immune system to recognize and kill tumor and infected cells, materializing an old dream of regulating the immune system to cure patients [3,6].

PD-1 (also known as CD279) belongs to the B7-CD28 family of receptors [2,7]. The protein binds to two ligands, namely PD-L1 (B7-H1 or CD274) and PD-L2 (B7-DC or CD273). Upon binding to either of its two ligands, PD-1 provides co-inhibitory signals to TCR or BCR crosslinking and promotes for immune tolerance [8,9]. Contrary to the rest of the B7-CD28 receptors whose expression is restricted to the activated T cells, PD1 is also expressed on B cells, NK and NKT cells as well as in dendritic cells (DCs) [10]. Likewise, there is a substantial difference in the expression of its two ligands. While PD-L1 is expressed in many cells including T and B cells, DCs, macrophages and nonhematopoietic cells, PD-L2 however, is only expressed on a subset of B cells and can be induced on DCs, monocytes and macrophages in a cytokine-dependent manner [10].

* Corresponding author at: Faculty of Pharmacy and Pharmaceutical Sciences, University of Alberta, Edmonton, AB, Canada. Tel.: +1 7804925783.
E-mail address: Kbarakat@ualberta.ca (K. Barakat).

http://dx.doi.org/10.1016/j.jmgm.2015.01.015
1093-3263/© 2015 Elsevier Inc. All rights reserved.

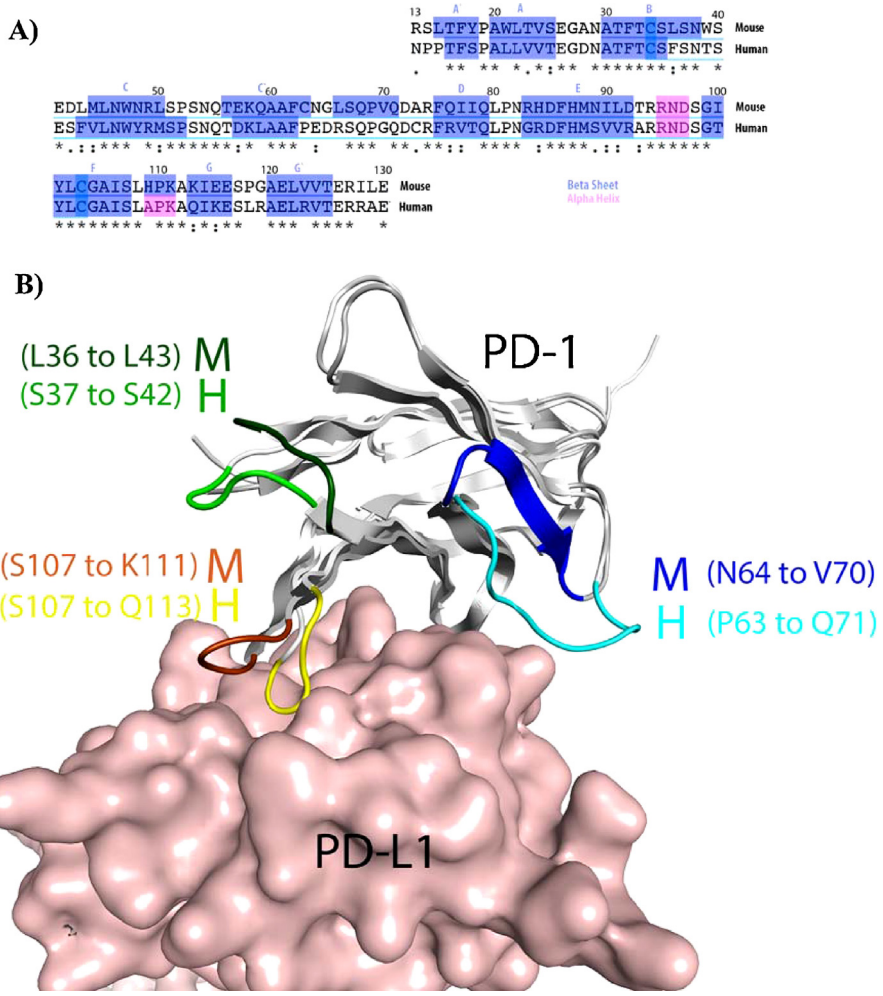

Fig. 1. Sequence and structural alignments between human and mouse PD-1. (A) The two proteins have ~65% sequence identities, with their major differences are imposing more flexibility to the human PD-1. (B) PD-L1 is shown in a surface representation and colored in pink. Regions that are not forming the binding interface with PD-L1 are quite similar in both human and mouse PD-1 (colored in white). The major differences between the two proteins are at the binding interface with the ligand. The most important variations are the lack of a beta strand (dark blue) present in the mouse structure that is replaced with a long flexible loop (light blue), the more flexibility in the loop formed by residues S107 to Q113 (yellow) and the loop between residues S37 to S42 in human PD-1 (light green). (For interpretation of the references to color in this figure legend, the reader is referred to the web version of the article.)

PD-1 is a monomeric type I surface transmembrane glycoprotein comprising 118 amino acids (see Fig. 1A). The protein is organized in four domains including a single V-set immunoglobulin superfamily (IgSF) domain, a stalk of 22 residues, a transmembrane domain and a 95 residues cytoplasmic domain, which contains two tyrosine-based immunoreceptor signaling motifs; the inhibitory motif (ITIM) and the switch motif (ITSM). Although the two PD-1 ligands share only 34% identity with each other, they carry the same structural signature of the rest of the B7 ligands. Their extracellular domains include a tandem V-set motif, which directly interact with PD-1 and a C1-set IgSF motif. PD-L1 and PD-L2 are type I transmembrane proteins comprising 290 and 270 residues respectively. They both possess a conserved short intracellular domain (only ~30 residues) with not yet known functions. Interestingly, besides PD-1, PD-L1 was found to bind B7-1 (CD80), probably, as a developed mechanism to link the PD-1 and the CD28/CTLA-4 signaling pathways [11].

Despite the reported significant success of current agents blocking the PD-1 pathway, all of these agents are monoclonal antibodies that are directed toward either PD-1 (e.g. nivolumab [12], lambrolizumab [13] and MEDI4736 [14]) or PD-L1 (MPDL3280A [15]). These agents not only proved the concept for this approach, but also they fueled the enthusiasm toward rationally designing small molecules targeting this pathway [16]. Nevertheless, there have not been any reported success stories with this regard in the literature. This is due to the limited information concerning the structural interactions between PD-1 and its two ligands. Current crystal structures describe the interactions of mouse PD-1 with human PD-L1 [17] or mouse PD-L2 [18]. There is no crystal structure for these interactions with human PD-1 and any of its two human ligands. The lack of these structures constitutes a high barrier against rationally developing small molecules targeting these interactions. This is mainly due to the sequence identity difference between mouse and human, which affects the PD-1 binding conformations to any of its ligands as well as altering their binding interfaces (i.e. close an otherwise open binding pocket). Wang et al. made the first attempt to cross this barrier by reporting homology models for human PD-1 ligands. They combined these models with mutational analysis to roughly map the PD-1 binding interface within PD-L1 and PD-L2 [19]. A more recent study by Cheng et al. provided a preliminary model for human PD-1 bound to each of its human ligands [20]. They used the mouse crystal structures described above and superimposed them to their human PD-1 model. Although these two earlier studies by Wang and Cheng presented an initial guess for the interaction of PD-L1 and PD-L2 with the PD-1 receptor, there were some discrepancies between these models and available nuclear

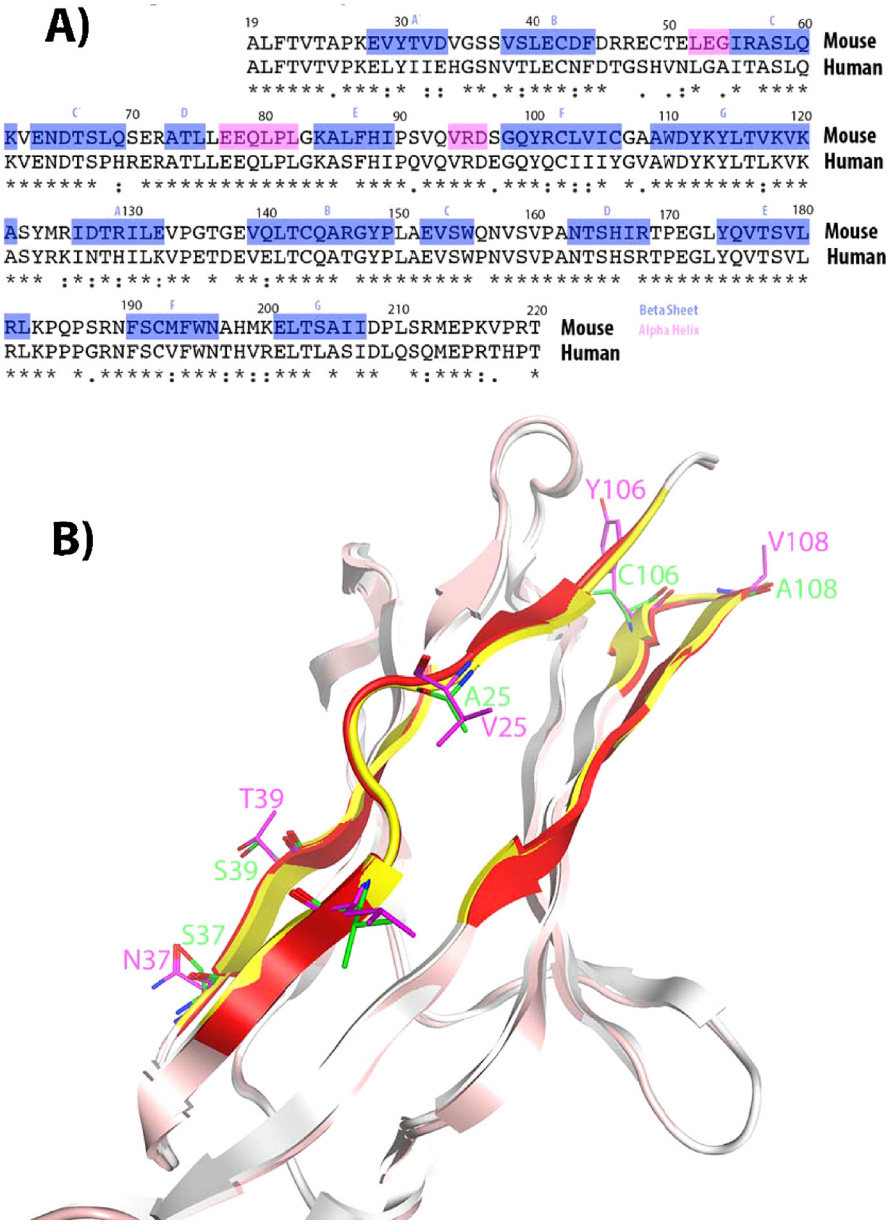

Fig. 2. Sequence and structural alignments between human and mouse PD-L2. (A) Sequence alignment of the two proteins indicates that human and mouse PD-L2 have 73.3% identity and all the sequence differences are residue substitutions with no missing residues. (B) The binding interface to PD-1 of both human (yellow for mouse and red for human) and mouse PD-L2 are quite similar with very few mutations (green for mouse and pink for human). Residues far from the binding interface are represented by newcartoon and colored in white for the mouse and light pink for human. (For interpretation of the references to color in this figure legend, the reader is referred to the web version of the article.)

magnetic resonance (NMR) and mutational analysis data that still need to be addressed [20].

Here we describe for the first time two accurate models for human PD-1 bound to its two human ligands, namely PD-L1 and PD-L2. Our methodology involves combining molecular dynamics (MD) simulations with protein–protein docking and binding energy analysis to predict the most probable binding conformation of PD1 to its ligands. The docking simulations were guided by our knowledge of the binding interface based on available crystal structures [17,18], Cheng's NMR data [20] and Wang's mutational analysis [19]. Extensive MD simulations were used first to generate an ensemble of protein structures for the three molecules, followed by docking the generated protein structures and coarsely ranking the docking results based on their matching to the available experimental data. Top hits were then subjected to a second round of MD simulations to relax their binding interfaces and prepare them for binding energy analysis using the molecular mechanic-Poisson Boltzmann surface area (MM-PBSA) method [21–28]. Results described below reveal the most accurate atomistic details of how human PD-1 binds to human PD-Ls and why the two ligands bind with different affinities to the same receptor.

2. Results

2.1. Sequence alignment and homology modeling

Human and mouse PD-1 share many conserved residues (~65% identity). Most of these conserved residues are located within the B, F and G′ strands (see Fig. 1A). The two structures also incorporate a conserved disulfide bond between C34 from the B strand with the C103 from the F strand. This disulfide bond stabilizes the two beta sheets GFCC′ and ABED in both human and mouse PD-1. There are

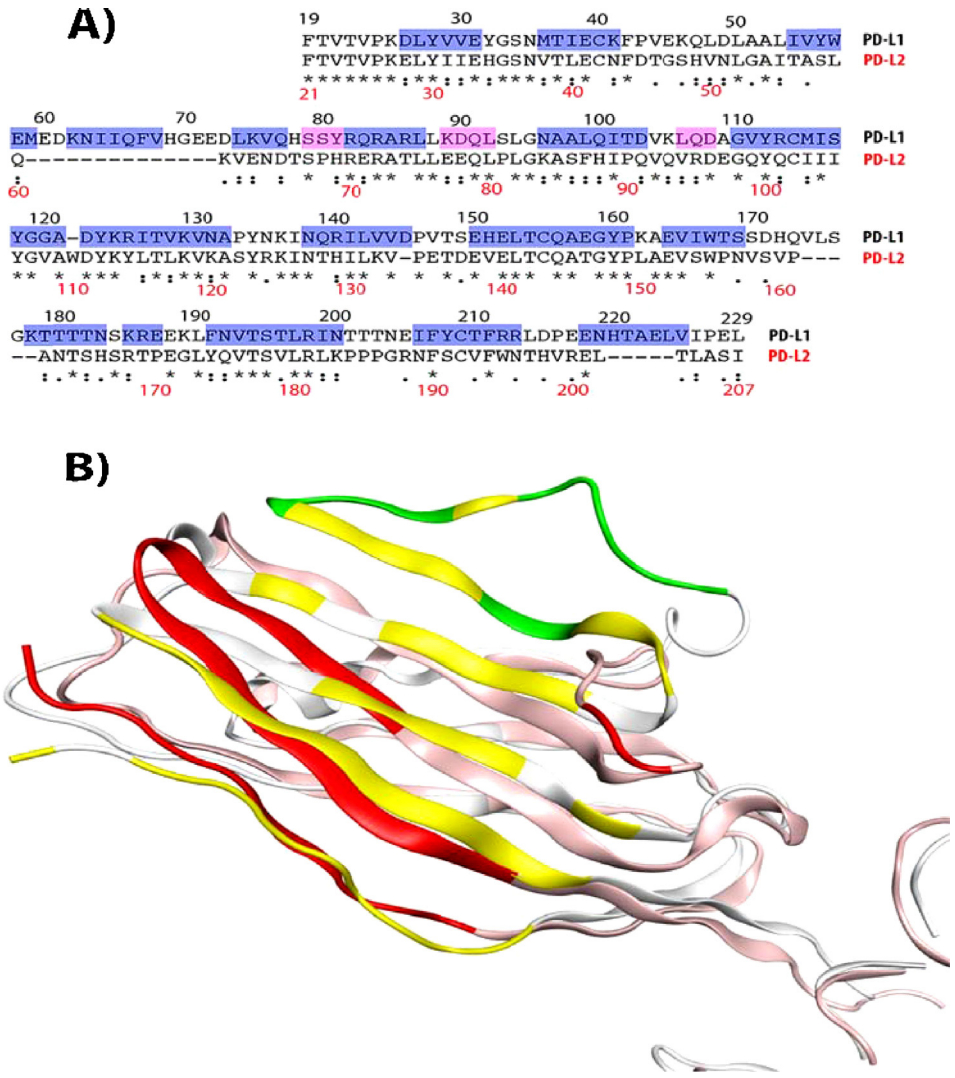

Fig. 3. Sequence and structural alignments between human PD-L2 and human PD-L1. (A) The two proteins have only 34% sequence similarity. PD-L2 is missing many residues compared to PD-L1 including the C′ strand. (B) The binding interface to PD-1 in PD-L1 (yellow) and PD-L2 (red) with the missing loop and strand are highlighted with green. Residues far from the binding interface are represented by newcartoon and colored in white for the PD-L1 and light pink for PD-L2. (For interpretation of the references to color in this figure legend, the reader is referred to the web version of the article.)

no missing residues between mouse and human PD-1 and all the differences among the aligned residues are mainly substitutions. Superposition of the two structures reveals their high degree of structural similarity (see Fig. 1B). Most of the structural variations are limited to residues F36–F43 (B-C loop), E64–G70 (C′-D loop) and S107–K111 (F-G loop). These flanked regions show extra flexibility in the human PD-1 compared to those in the mouse structure, particularly, for the C′-D loop which involves a structured beta strand in the mouse model that is completely absent in human PD-1. These local variations directly affect the conformational dynamics of the binding interface of PD-1 to its two ligands (see Fig. 1B) and investigating their dynamical behavior was essential to discover the correct mode of binding of human PD-1 to its two human ligands (see below).

Fig. 2A illustrates the sequence alignment of human and mouse PD-L2. The two structures are quite similar with almost 75% identity. Analogous to the human and mouse PD-1, human PD-L2 has no missing residues from the mouse structure and all their differences are based on residue substitutions. Their high degree of similarity made the mouse structures the most appropriate template to construct a homology model for human PD-L2. As shown in Fig. 2B, the PD-1 binding interface within PD-L2 is highly conserved between human and mouse, indicating a similar mode of binding to PD1 for the two species. With the exception of Y106 in human PD-L2, which is mutated into a cysteine residue, the rest of the mutations yielded structurally similar substitutions that would not significantly affect the mode of PD-L2 binding to PD-1 and limit these effects to the aforementioned local changes between human and mouse PD-1 as described below.

Comparing PD-L1 to PD-L2 revealed significant differences between the two proteins. Although the IgC domains of the two protein ligands are structurally similar, their IgV domains, which interact with PD-1, are clearly different (see Fig. 3). For example, human PD-L2 lacks the C′ beta strand found in human PD-L1 which directly interacts with PD-1 in our model (see below). This prominent variation along with the many mutations that are distributed within the two structures (see Fig. 3B) resulted in two different binding interfaces for PD-1 to the two ligands as described below.

2.2. Molecular dynamics (MD) simulations on the apo structures

Proteins are dynamical entities and their dynamical behavior is essential for their proper function, particularly, when they form protein–protein complexes. To explore the conformational

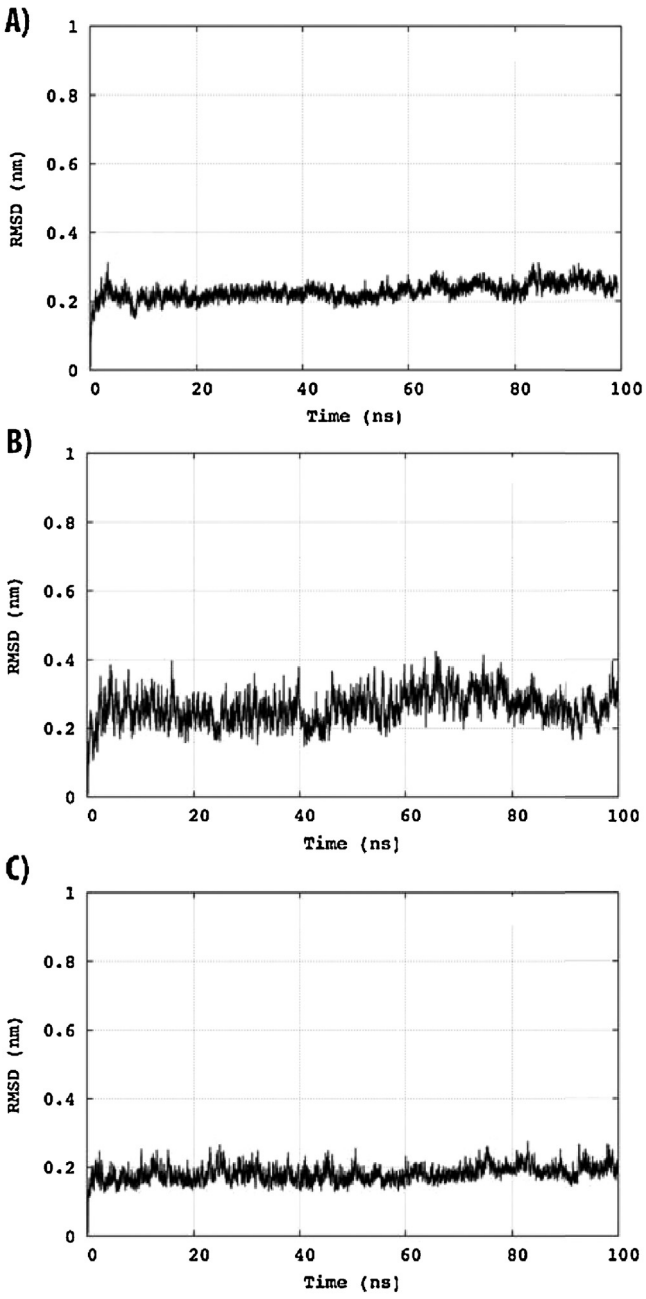

Fig. 4. Root mean square deviations (RMSD) for the three 100 ns MD simulations. (A) PD-1, (B) PD-L1 and (C) PD-L2.

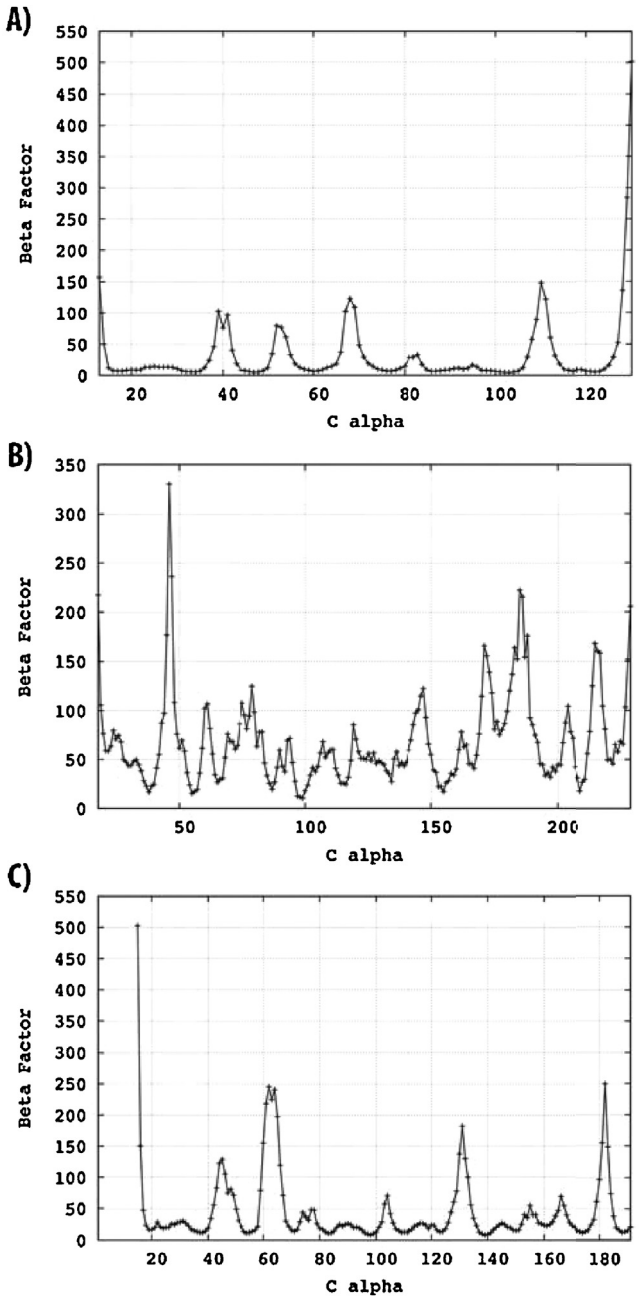

Fig. 5. Atomic fluctuations per reside for the three trajectories (A) PD-1 is mostly rigid except for residues at the binding interface of the two ligands. (B) PD-L1 is highly flexible compared to PD-L2 shown in (C).

dynamics of the three targets and to prepare an ensemble of structures suitable for subsequent docking simulations, we run three 100 ns MD simulations on the apo (unbound) PD-1, PD-L1 and PD-L2 proteins. Fig. 4 displays the root mean square deviations (RMSD) of the three trajectories, revealing their stability. The atomic coordinates of the three proteins fluctuated almost around 0.2 nm, similar to other previously reported protein dynamics [29–31]. Interestingly, PD-L1 showed more atomic fluctuations compared to PD-L2, reflecting the structural variations between the two proteins as described above. These vibrant dynamical differences are also revealed when comparing the atomic fluctuations (beta factors) for the three proteins (See Fig. 5). PD-L2 showed more rigidity compared to PD-L1, which showed large flexibility in almost all domains, particularly, between residues E41 to Q49; E140 to F190. On the other hand and similar to PD-L1, PD-1 showed almost rigid behavior, except for the loops that are formed between residue intervals F36 to C42l; M50 to Q56; R66 to Q71 and I106 to Q113.

2.3. Extracting the dominant conformations for flexible docking

Current protein–protein docking algorithms poorly incorporate protein flexibility during the docking simulation [32]. In most cases, they perform rigid protein docking and in very limited algorithms only the side chains of residues at the interface are allowed to rotate, with the rest of the protein structure remains rigid during the docking process. This prevents the backbone dynamics of the two docked proteins from being properly included within docking. One way to get around this problem, as we adopted here, is to use an ensemble of structures for each docked protein. Each member of the receptor ensemble is docked to the individual structures

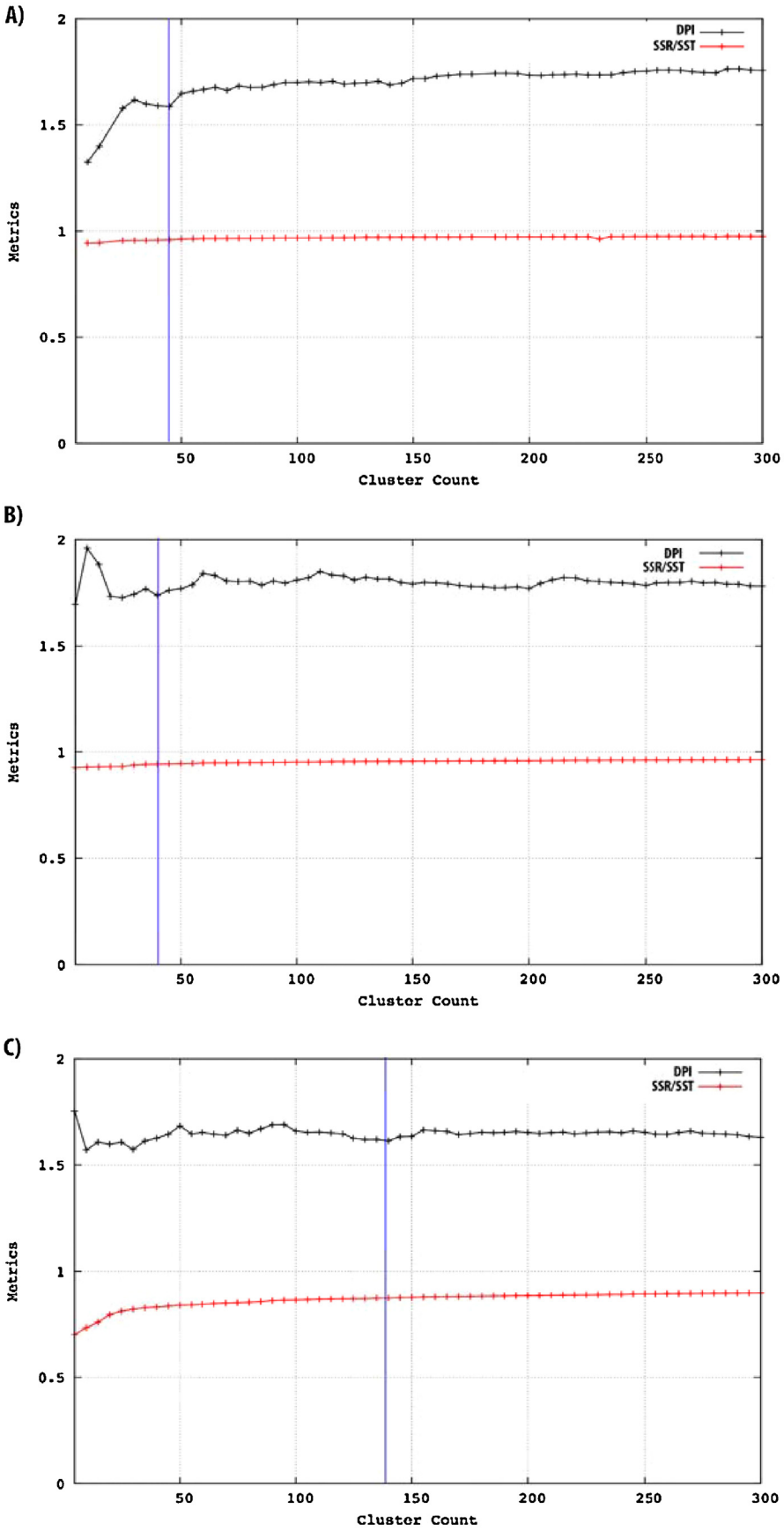

Fig. 6. Clustering analysis for the three trajectories. An optimal clustering number is predicted when a plateau in SSR/SST coincides with a local minimum in the DBI metric. This occurred for cluster counts of 45 for PD-1 (A), 65 for PD-L1 (B) and 145 for PD-L2 (C).

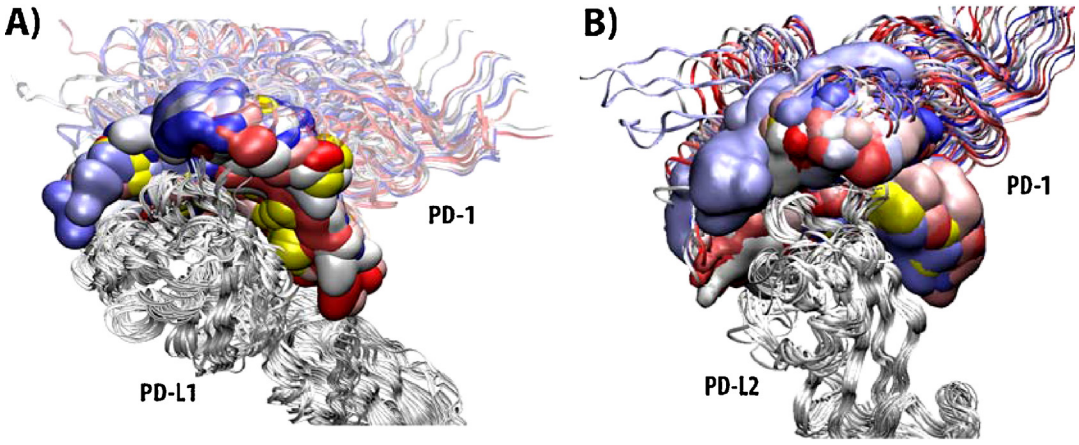

Fig. 7. Top hits from protein–protein docking for (A) PD-1/PD-L1 and (B) PD-1/PD-L2. The top hits are superimposed on each other and the ensemble-based docking simulations allowed the V domains of the three proteins to extensively explore all possible conformations. Residues from PD-1 at the binding interface are shown in surface representation and colored by a distinctive color with the best hit is shown in yellow. Residues outside the range of the binding interface are shown in ribbon representations.

from the ligand. Here, we constructed these ensembles from the MD simulations for each protein using an adaptive clustering technique that aims at extracting their dominant conformations at the optimal number of clusters (see Methodology). Fig. 6 shows the clustering analysis for the three MD simulations. By varying the number of clusters from 5 to 300 while observing the two clustering metrics DBI and SSR/SST (see methods), one expects a high quality clustering when a constant value of SSR/SST matches with a local minimum for the DBI, as this was the case for PD-1, PD-L1 and PD-L2 at 45, 65 and 140 clusters respectively. All possible combinations of these structural ensembles were considered during the docking simulations, however, the interaction surfaces of these proteins were constrained by our previous knowledge of the general regions of their contacts as described below.

2.4. Knowledge-based protein–protein docking

Performing protein–protein docking using the ensemble-based strategy described above required running 2925 and 6300 independent docking simulations for PD1/PD-L1 and PD-1/PD-L2 respectively. Each docking simulation, if not restricted to specific regions within the interacting proteins, would be required to explore an enormous search space that, in many cases, would result in irrelevant bound complexes (false positives). Therefore, it was important to limit the docked surfaces within each protein to those that can reveal realistic and physiologically relevant complexes. As PD-1 interacts through its V domain with the V domains of both PD-L1 and PD-L2, forming a pair of bound V domains in Fv-like structures, we decided to limit the search to these regions from each protein. To do that, we employed the ZDOCK protein–protein docking software [18,33,34], which besides its excellent docking algorithm and scoring method, also has the feature of blocking uninteresting residues, excluding them from the docking simulations and focusing only on important protein surfaces, thus; the conformational search is significantly lowered. The top 10 hits (based on ZDOCK scoring) for each docking simulation were then analyzed for their correlation with Cheng's NMR data [20] and Wang's mutational analysis [19], by scanning the distances of the reported residues and only retaining the complexes that have relevant locations of these residues at the binding interface. Limiting our search by these spatial constraints significantly reduced the number of the obtained docked structures from 29,250 and 63,000 complexes for PD1/PD-L1 and PD1/PD-L2 respectively, to manageable number for each protein–protein complex (see Section 4). Fig. 7 shows a superposition of the top hits for both PD1/PD-L1 and PD1/PD-L2. Incorporating the flexibility of the interacting proteins allowed the V domain of PD-1 to efficiently explore the whole surface of the V domains of PD-L1 and PD-L2. As shown in Fig. 7, backbone dynamics played an essential role in structurally fitting the interacting protein structures during docking, allowing the flexible loops at the interface to re-arrange and extensively visit all possible interactions. As shown in Fig. 7, all of the resulting top hits interacting through their V domains, have considerable spatial and orientational similarities, and all of them satisfy, to a high degree, the constraints imposed on known important residues. To finally select a model for each protein–protein complex, we decided to refine all these remaining hits through all-atom MD simulations with explicit solvent and ions followed by ranking them based on their binding affinities (see below).

2.5. Refining the docked structures and their final ranking

As expected, the MD simulations relaxed the protein–protein complexes of the docked structures. The equilibrated structures have closer contacts between the interacting domains, mainly at the binding interfaces. More importantly, the resulting MD trajectories allowed us to accurately measure the binding affinities for the predicted complexes using the molecular mechanic-Poisson Boltzmann surface area (MM-PBSA) method [21–28]. The MM-PBSA method has been successfully applied in several drug design related studies [35–42]. We also included for this analysis two models of PD-1/PD-L1 and PD1/PD-L2 that were constructed by superimposing the human PD-1, PD-L1 and PD-L2 on the reported mouse crystal structures for each protein–protein complex similar to the same procedure as described in Cheng's study [20]. This was important to compare the binding energies of the docked structures to those that are based on the mouse complexes and recognize how structurally far they are. Table 1 shows the ranking of the top hits for each docking simulation. The binding energies for the mouse-fitted models are also included for comparison. Although most of the resulted docking structures in both cases showed little structural shifts at the interfaces between the interacting proteins, these minor alterations seem to have considerable impact on their binding affinities, ranging from 3 to −44 kcal/mol and from 0 to −48 kcal/mol for PD-1/PD-L1 and PD-1/PD-L2, respectively. To gain further understanding on these significant alternations in the binding energies among the different models, we decomposed their binding affinities into residue contribution (see below). This was also important to identify the important residues and correlate their binding contribution with the available mutational and NMR

Table 1
MM-PBSA binding energies for the top hits from docking simulations compared to the mouse fitted structures.

Model #	PD-1/PD-L1 BE (kcal/mol)	PD-1/PD-L2 BE (kcal/mol)
Model 0	−20	−6
Model 1	−11	−16
Model 2	−36	−4
Model 3	−38	−4
Model 4	−17	−13
Model 5	−18	−23
Model 6	−28	−26
Model 7	−12	−7
Model 8	1	−4
Model 9	−16	−17
Model 10	−32	−14
Model 11	−11	−14
Model 12	−12	−19
Model 13	3	−5
Model 14	−11	−19
Model 15	−24	−4
Model 16	−24	−14
Model 17	3	−2
Model 18	−16	−21
Model 19	−8	−18
Model 20	−7	0
Model 21	−10	−10
Model 22	−8	−12
Model 23	−44	−11
Model 24	−4	0
Model 25	−12	−16
Model 26	−15	−15
Model 27	−33	−48
Model 28	−29	−26
Mouse-fitted (#29)	−34	−42

data. Nevertheless, the binding affinities of the final selected models (model 23 for PD-1/PD-L1 and model 27 for PD-1/PD-L2) suggest that PD-1 binds with more affinity to PD-L2 compared to PD-L1, as revealed by previously reported experimental findings [17,20].

2.6. hPD-1 binds differently to its two ligands

The binding interface in PD-L1 is larger than that in PD-L2, which lacks the C′ beta strand found in PD-L1. Therefore more residues are contributing to the binding energy in PD-L1 compared to PD-L2. Similarly, this required more residues from PD-1 to line up for interactions with PD-L1 compared to the case for PD-L2. The energy contributions per residue varied from −12 to 4 kcal/mol for PD-1/PD-L1 models and from −10 to 6 kcal/mol for PD-1/PD-L2 structures (data not shown). Figs. 8 and 9 represent the major findings of the present study and show the structural differences between our top hits compared to the mouse-fitted structures for PD-1/PD-L1 and PD-1/PD-L2 respectively as well as the predicted binding modes of PD-1 to its two ligands. As expected from the aforementioned analysis, PD-1 binds differently to its two ligands. While PD-1 has a major conformational change compared to the mouse-fitted structure in binding to PD-L1 (see Fig. 8), it has a very similar mode of binding with the mouse-fitted model in PD-L2 (see Fig. 9). The flexibility of the two loops (formed by residues D65 to Q71; and L108 to I114) from PD-1 appears to play an important function in readjusting the beta sheets of the PD-1V domain to interact with the two different ligands. More importantly, as indicated above, the two loops form a major difference between human PD-1 and its mouse counterpart, with the loop formed by residues D65 to Q71, for example, is replaced by a beta sheet in the mouse model (N64 to V70). These flexible loops in human PD-1 interacted directly and differently with the two ligands, as in the case of PD-L2 where the two loops had very close interactions within the binding interface, whereas, they had limited interactions with PD-L1.

3. Discussion

Programmed death-1 (PD-1) is a potent inhibitory receptor of T cells and a sustained expression of PD-1 is directly associated with T cells' dysfunction, leading to a state of immune tolerance to tumors and chronic infections [43]. PD-1 induces its activity through binding to either one of its two ligands, namely PD-L1 (also known as B7-H1 or CD274) and PD-L2 (also known as B7-DC or CD273) [8]. Blocking these interactions showed outstanding promise in restoring T cells' activity and reactivating the immune system to recognize and eradicate tumor and infected cells [5]. Current agents targeting these interactions are limited to monoclonal antibodies and despite their huge therapeutic potential the rational design of more effective agents (i.e. small molecule inhibitors) is restricted by the limited knowledge on how these proteins interact. Available crystal structures only describe the interactions of mouse-PD-1 with human-PD-L1 [17] or mouse-PD-L2 [18]. The detailed and accurate picture of how human-PD-1 interacts with either human-PD-L1 or human-PD-L2 is still missing, preventing further utilization of this influential immunotherapeutic pathway. Two earlier studies tried to answer this question. Wang et al. combined homology modeling with site-directed mutagenesis to map the binding interface of PD-1 to its two ligands. Although a number of their suggested mutations correctly influenced the binding affinity of PD-1, the models described in their study only provide a preliminary description of these interactions as they relied on templates that have only ∼16% similarity with PD-Ls. These models also did not elucidate the direct interaction between PD-1 to its ligands by showing how these complexes are formed and oriented in 3D. Cheng et al. executed a more recent study exploiting the available crystal structures for mouse-PD-1 with human-PD-L1 [17] and mouse-PD-L2 [18] and employing nuclear magnetic resonance (NMR) chemical shift analysis to identify residues at the binding interface of both PD-1/PD-L1 and PD-1/PD-L2. To build two models for the complexes between PD-1 and the two ligands, they basically superimposed their experimentally determined structure for human-PD-1 on the mouse PD-1 structures, assuming that human-PD-1 would have similar mode of binding to the mouse structures. However, as they indicated in their study and as we found here, this is not the case. Their mouse-superimposed models could not fit completely to the NMR data with various inconsistencies that we tried here to understand their structural origin and construct new models that can better describe these data. In the current study, we combined state-of-the-art molecular dynamics simulations with protein–protein docking and binding energy analysis to predict the most probable modes of binding of PD-1 to its two ligands. Similar to the workflow described herein, Xu et al. recently characterized the protein–protein interactions between CXCR4 and its natural ligand CXCL12/stromal-derived factor-1 (SDF-1) [44]. Here we follow a similar but more extended approach to further address protein dynamics within docking simulations. We also built upon Wang and Cheng studies by utilizing their mutational and NMR analysis as a constraint for our modeling algorithm to select only the models that would fit best to these data followed by refinement of the retained models using molecular dynamics simulations.

The major differences between mouse and human PD-1 are at the binding interface with the two ligands. A striking difference is the missing C″ strand in human PD-1 that is found in the mouse structure. The well-structured strand is replaced with a long flexible loop in the human structure (see Fig. 1). Accordingly, human-PD-1 is more flexible at the binding interface compared to its mouse counterpart, indicating the likelihood of having a different mode of binding to the two ligands. Similarly, the major differences between human-PD-L1 and human-PD-L2 are also at their binding interface with PD-1. Although the two ligands share several conserved residues at the PD-1 interface, human PD-L2

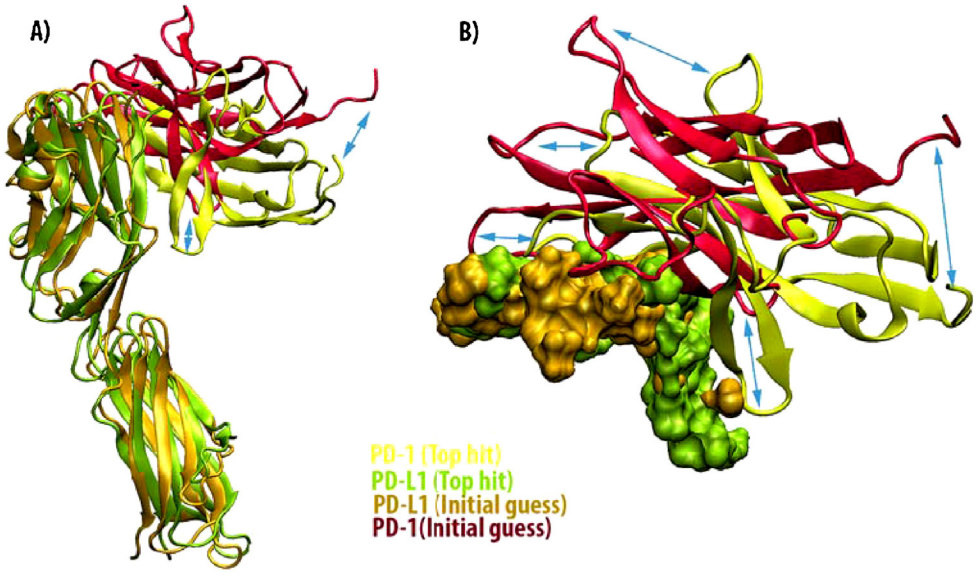

Fig. 8. Interaction between PD-1 and PD-L1. (A) Compared to the mouse-fitted (PD-1 shown in red and PD-L1 in orange) structure, the human (PD-1 shown in yellow and PD-L1 in green) binding mode of PD-1to PD-L1 has a major conformational change from that in the mouse. (B) The binding interface in PD-L1 is shown in molecular surface representation and colored in green for top hit and in orange for the mouse-fitted model. PD-1 is shown in newcartoon representation and colored in red for the mouse-fitted structures and in yellow for the top hit from docking. Arrows 1 point out to the regions with significant conformational changes between the two cases.

lacks the C′ beta strand found in human PD-L1 which directly interacts with PD-1, suggesting the two ligands would bind differently to the same receptor.

Our models shown in Figs. 8 and 9 show how human-PD-1 interacts differently with its two human-ligands. Moreover, they also compare these binding modes to the mouse-fitted structures described in Cheng's study. Interestingly, our human-PD-1/human-PD-L1 model reveals a major conformational change from the mouse-fitted complex. As expected, these major changes are mainly due to the rearrangements of the loops between the C′D strands and the BC strands in PD-1. The mouse-fitted structure for PD-1 bound to PD-L1 was energetically unfavorable by ~10 kcal/mole compared to the predicted model. On the other hand, our model for human-PD-1 bound to human PD-L2 indicates that the human structures has a minor conformational change compared to the mouse models, with only 4 kcal/mol in favor of our model. Our modeling also suggests that PD-L2 binds stronger to PD-1 than PD-L1, correlating with available binding affinity studies [17,20]. Binding energy decomposition analyses for the two protein–protein complexes indicate that the PD-1-binding interface on the surface of PD-L2 is larger than that on PD-L1. More importantly, residues shown to contribute significantly to the binding energies correlate well with Cheng's NMR data. For example, for the PD-1/PD-L1 complex, PD-1 residues Q55 to K58 from the C′ strand, L102 to A105 from the F strand and A112 to E116 from the FG loop are directly at the binding interface within less than 4 Å of

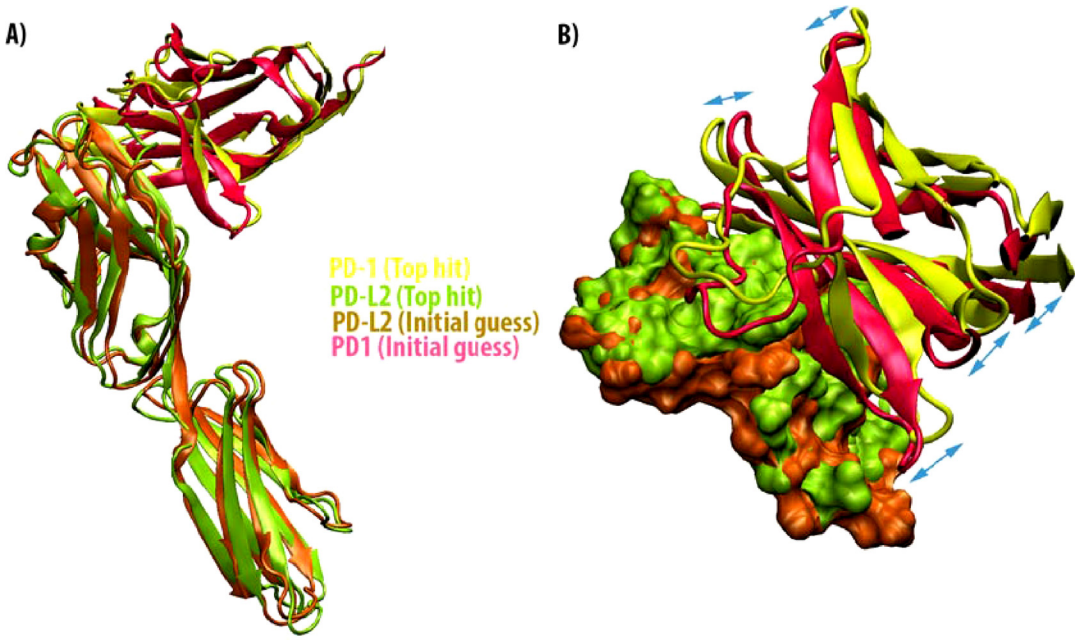

Fig. 9. Interaction between PD-1 and PD-L2. The color codes and representations are the same as that of Fig. 8. (A and B) hPD-1 and hPD-L2 have a very similar mode of binding compared to the mouse-fitted structure with very minor conformational changes.

PD-L1. Additionally, as a main benefit of incorporating protein flexibility within docking in our model, residues F43 to N46 from the PD-1 C strand interact with both ligands, outlining a major difference from the mouse-fitted structures and solving one of the NMR structural discrepancies in Cheng's study [20], which lack these interactions, predominantly for the PD-L1 case. In addition to NMR data, which mainly focused on the interface residues from the PD-1 side, previously reported mutational analysis identified a number of residues in the two ligands that seem to be essential for the interaction with PD-1 [19]. Among these residues is W110 from PD-L2, which contributed around −12 kcal/mol to the binding affinity of PD-L2 to PD-1 (data not shown). It is important to emphasize here that this residue is missing in PD-L1 (see Fig. 2), which may account for the lost 10 kcal/mol in the PD-1/PD-L1 complex. In the PD-1/PD-L2 complex, W110 is totally hidden underneath the F strand of PD-1, mainly interacting with G104 and A105 from PD-1. Other important residues include D111, K112 and Y113 in PD-L2 (corresponding to D123, K124 and Y125 in the G strand of PD-L1). The conservative nature of these residues between PD-L1 and PD-L2 suggests that their important roles in forming the binding interface with PD-1.

The models described herein are consistent with the available experimental data and provide the most detailed 3D picture, so far, for the interactions of human-PD-1 with its two human-ligands. These models also provide the tools to fully use this unique immunotherapeutic pathway and rationally develop more effective and safer drugs to block the protein–protein interactions involved in this pathway (work in progress).

4. Materials and methods

4.1. Homology modeling of hPD-L2

To generate the structure for human PD-L2, we used the homology-modeling module as implemented in the molecular operating environment (MOE) software (http://www.chemcomp.com). The amino acid sequence for hPD-L2 (Q9BQ51) was retrieved from the Protein Knowledge database (UniProtKB: http://www.uniprot.org/) and the MOE-SearchPDB module was then used to scan the Protein Data Bank database (PDB) for suitable templates. As expected, MOE identified chain B from PDB entry 3BP5 (the mouse PD-L2; resolution = 1.8 Å) as the most similar structure for hPd-L2 (73.3% identity). Interestingly, there were no gaps in the human sequence compared to the mouse version and all the mismatched residues were substitutions. As the mouse template included all the required residues for PD-1 binding, the amino acids of hPD-L2 that extended beyond the template sequence in the alignment were clipped off before the models was built. Fifty hPDL-2 models were independently generated by MOE based on Boltzmann-weighted randomized procedure and avoiding steric clashes for the substituted residues by exploring the rotamer databases for the conformations of their side chains. The Fifty models were then minimized for 5000 steps of steepest descent followed by conjugate gradient minimization until the RMS energy gradient was lower than 0.01 kcal/mol/Å. All the models were then ranked by their packing quality function and Ramachandran plots. The best model was then selected as a preliminary structure for hPDL-2 and was subjected to extensive MD simulations for model refinement and conformational analysis (see below).

4.2. Molecular dynamics simulations

Similar to previously published work [29,45–47], all protein structures were subjected to MD simulations at a mean temperature of 310 K and physiological pH (pH 7). The NAMD software [48] was used to run all the MD simulations with the all-hydrogen AMBER99SB force field [49]. The protonation states of ionized residues for each protein structure were predicted using the PDB2PQR software [50]. All systems were explicitly solvated in a TIP3P water cube to provide at least a 12 Å wide buffer of water molecules around the systems. Upon solvation, each system was electrostatically neutralized under a physiological ionic concentration, of chloride and sodium ions. The number of counter-ions for each case was calculated by first estimating the number of ions that are needed to set up the solvated system under normal physiological conditions (pH 7), followed by adding the number of chloride ions required to bring the net charge of the total system to zero. Overall, 63 MD simulations were carried on in this work. Three extensive MD simulations were run on the apo hPD1, hPD-L1 and hPD-L2 protein structures to generate an exceptionally long trajectory (100 ns) in order to explore their conformational dynamics for subsequent docking simulations (see below). Two additional 15 ns MD simulations were run on the h-PD-1 bound to its two human ligands after aligning the human structures with the mouse crystal structures. Finally, as a post-processing to the docked protein complexes, we run 58 15 ns MD simulations on the top 58 hits from docking simulations.

The following protocol was used for all MD simulation described above. All systems were first minimized and subsequently heated to the simulation temperature with heavy restraints placed on all backbone atoms. Following heating, the systems were equilibrated using periodic boundary conditions for 100 ps and energy restraints reduced to zero in successive steps of the MD simulation. The systems were then continued for the simulations' times described above. For binding energy analysis, atomic coordinates of complexes from their last 10 ns MD simulations were saved to the trajectory every 10 ps. That is, for each protein–protein case we obtained 1000 snapshots from the simulation. This time interval was selected to be twice the largest correlation time to ensure that all binding energy data are uncorrelated. The root-mean-square deviations (RMSD) and B-factors were computed over the duration of the simulation time using the PTRAJ utility within AMBER12. Hydrogen bond analyses were performed by computing the average distance between donor and acceptor atoms. A hydrogen bond was defined by a heavy donor – heavy acceptor distance $\leq$3.4 Å, a light donor-heavy acceptor distance $\leq$2.5 Å, and a deviation of less than $\pm 40^{\circ}$ from linearity.

4.3. Clustering analysis

As previously described in details, here we used an in-house automated methodology for clustering of MD trajectories while predicting the optimal number of clusters [39,47,51]. Briefly, clustering analysis was preformed on the three apo structures (hPD-1 and its two ligands) for different numbers of cluster counts ranging from 5 to 300 clusters each using the average linkage algorithm as implemented in the PTRAJ utility of AMBER12. To remove the translational and rotational motions, all C_{α}-atoms were RMSD fitted to the minimized initial structures. The clustering quality was anticipated by calculating two clustering metrics, namely, the Davies-Bouldin index (DBI) [52] and the "elbow criterion" [53]. A high-quality clustering quality is obtained when DBI experiences a local minimum versus the number of clusters used. This is usually confirmed by the elbow criterion, in which the percentage of variance explained by the data is expected to plateau for cluster counts exceeding the optimal number of clusters [53]. Using these two metrics and by varying the number of clusters, we determined the optimal number of clusters for the three trajectories and extracted the representatives of these clusters as the dominant conformations for each system for subsequent docking (see Section 2).

4.4. Protein–protein docking

We used ZDOCK [54–59] to carry out the protein–protein docking simulations of PD-1 to its two ligands. ZDOCK performs rigid-body docking by exploring both the rotational and translational degrees of freedom of the protein structures. The software employs a Fast Fourier Transform algorithm (FTT) to speed up the docking process. It projects both the ligand and receptor protein structures onto 3D grids, attributing different values for each grid point relative to its allocation within the protein structures (e.g. interior, exterior or on the surface of the protein). ZDOCK then uses two discrete functions that describe the shapes of the ligand and receptor to calculate their overlap (i.e. their two grids) giving every docking trail a particular score, which penalizes any penetration at the interface of the two proteins. The score also includes electrostatics and solvation contributions. The higher the score, the better the docking result. ZDOCK also can restrain the docking search space to certain regions of the two proteins by blocking the none-interacting residues during the docking process. Using the obtained clustered ensemble structures for PD-1, PD-L1 and PD-L2 (see above), we ran 2925 and 6300 independent docking simulations for PD-1/PD-L1 and PD-1/PD-L2 respectively. Each docking simulation retrieved 10 top hits based-on ZDOCK scoring, and all these hits were then analyzed and compared to the available NMR and mutational analyses using an automated algorithm which calculates the distances between the reported important residues within the interacting proteins. After applying this initial filtering scheme, only 239 and 50 hits remained from the PD-1/PD-L1 and PD-1/PD-L2 docking results, which were then inspected through visualization to select only the complexes that show proper interactions of the V domains. The top 29 remaining hits based on the distance and visualization filtering were retained for MD simulations followed by binding energy analysis.

4.5. Binding energy analysis

We employed the molecular mechanic-Poisson Boltzmann surface area (MM-PBSA) method [21] to estimate the binding affinities for the docked protein–protein complexes and accurately rank their docking results. We used the same parameters as described in the literature [41,60–62]. The total free energy for each system was estimated as the sum of the average molecular mechanical gas-phase energies (E_{MM}), solvation free energies (G_{solv}), and entropy contributions ($-TS_{solute}$) of the binding reaction:

$$G = E_{MM} + G_{solv} - TS_{solute} \quad (1)$$

The molecular mechanical (E_{MM}) energy of each snapshot was calculated using the SANDER module of AMBER10. The solvation free energy (G_{solv}) was estimated as the sum of electrostatic solvation free energy, calculated by the finite-difference solution of the Poisson–Boltzmann equation in the Adaptive Poisson-Boltzmann Solver (APBS) and non-polar solvation free energy, calculated from the solvent-accessible surface area (SASA) algorithm. The solute entropy was approximated using the normal mode analysis. For each protein–protein complex, the binding free energy was approximated by the difference between the bound and free systems:

$$\Delta G^0 = \Delta G_{gas}^{PD-1/PD-L} + \Delta G_{solv}^{PD-1/PD-L} - (\Delta G_{solv}^{PD-L} + \Delta G_{solv}^{PD-1}) \quad (2)$$

Similar to the work described by Genheden and Ryde [63], based on estimating the correlation time between the different snapshots, we selected only 1000 structures from each trajectory to predict the molecular mechanics and solvation contributions. Due to the required computational time and resources for the entropy contribution, we used only 50 snapshots for each system for this purpose.

5. Conclusion

A sustained activation of the programmed death-1 (PD-1) pathway inhibits T cells' activity, leading to a state of immune tolerance. Tumors and infectious diseases can hide from the immune system by stimulating this potent immunoregulatory inhibitor and blocking this pathway emerged as a 'game changer' approach in cancer immunotherapy. The PD-1 receptor binds two ligands, namely PD-L1 and PD-L2 and upon binding to either of the two ligands, PD-1 provides co-inhibitory signals to TCR or BCR crosslinking and promotes for immune tolerance. Although the binding interface between PD-1 and its two ligands is broadly known to be through their V domains, the detailed mode of binding, particularly, for human variants is not fully understood. Current crystal structures describe the interactions of mouse PD-1 with human PD-L1 or mouse PD-L2. There is no crystal structure for these interactions with both human PD-1 and any of its two human ligands and recent NMR and mutational analysis suggest that their mode of binding in human is different from that in mouse.

Here, we present for the first time two accurate models for human PD-1 bound to its two human ligands. Our methodology involved combining molecular dynamics (MD) simulations with protein–protein docking and binding energy analysis to predict the most probable binding conformations for PD1 to its ligands. Results described herein remove the barrier against rationally developing more effective and safer agents targeting the PD-1 pathway by revealing the most accurate so far atomistic details of how human PD-1 binds to human PD-Ls and why the two ligands bind with different affinities to the same receptor.

Authors' contributions

The manuscript was written through contributions of all authors.

Conflict of interest statement

The authors declare no competing financial interest.

Acknowledgment

All the computational simulations have been accomplished on the SHARCNET and WESTGRID computer clusters in Compute Canada.

References

[1] B. Merelli, D. Massi, L. Cattaneo, M. Mandala, Targeting the PD1/PD-L1 axis in melanoma: biological rationale, clinical challenges and opportunities, Crit. Rev. Oncol. Hematol. 89 (2014) 140–165.
[2] A. Domling, T.A. Holak, Programmed death-1: therapeutic success after more than 100 years of cancer immunotherapy, Angew. Chem. Int. Ed. Engl. 53 (2014) 2286–2288.
[3] A.M. Intlekofer, C.B. Thompson, At the bench: preclinical rationale for CTLA-4 and PD-1 blockade as cancer immunotherapy, J. Leukoc. Biol. 94 (2013) 25–39.
[4] R.J. Greenwald, G.J. Freeman, A.H. Sharpe, The B7 family revisited, Annu. Rev. Immunol. 23 (2005) 515–548.
[5] C. Robert, J.C. Soria, A.M. Eggermont, Drug of the year: programmed death-1 receptor/programmed death-1 ligand-1 receptor monoclonal antibodies, Eur. J. Cancer 49 (2013) 2968–2971.
[6] M. Zhang, S. Maiti, C. Bernatchez, H. Huls, B. Rabinovich, et al., A new approach to simultaneously quantify both TCR alpha- and beta-chain diversity after adoptive immunotherapy, Clin. Cancer Res. 18 (2012) 4733–4742.
[7] L. Chen, Co-inhibitory molecules of the B7-CD28 family in the control of T-cell immunity, Nat. Rev. Immunol. 4 (2004) 336–347.
[8] T. Okazaki, T. Honjo, The PD-1-PD-L pathway in immunological tolerance, Trends Immunol. 27 (2006) 195–201.
[9] K.J. Lafferty, A.J. Cunningham, A new analysis of allogeneic interactions, Aust. J. Exp. Biol. Med. Sci. 53 (1975) 27–42.
[10] M.E. Keir, M.J. Butte, G.J. Freeman, A.H. Sharpe, PD-1 and its ligands in tolerance and immunity, Annu. Rev. Immunol. 26 (2008) 677–704.

[11] M.J. Butte, M.E. Keir, T.B. Phamduy, A.H. Sharpe, G.J. Freeman, Programmed death-1 ligand 1 interacts specifically with the B7-1 costimulatory molecule to inhibit T cell responses, Immunity 27 (2007) 111–122.
[12] G. O'Sullivan Coyne, R.A. Madan, J.L. Gulley, Nivolumab: promising survival signal coupled with limited toxicity raises expectations, J. Clin. Oncol. 32 (2014) 986–988.
[13] O. Hamid, C. Robert, A. Daud, F.S. Hodi, W.J. Hwu, et al., Safety and tumor responses with lambrolizumab (anti-PD-1) in melanoma, N. Engl. J. Med. 369 (2013) 134–144.
[14] C.J. Langer, Emerging immunotherapies in the treatment of non-small cell lung cancer (NSCLC): the role of immune checkpoint inhibitors, Am. J. Clin. Oncol. (2014), http://dx.doi.org/10.1097/coc.0000000000000059, http://journals.lww.com/amjclinicaloncology/pages/articleviewer.aspx?year=9000&issue=00000&article=99274&type=abstract
[15] B.C. Creelan, Update on immune checkpoint inhibitors in lung cancer, Cancer Control 21 (2014) 80–89.
[16] K. Barakat, Editorial: do we need small molecule inhibitors for the immune checkpoints? J. Pharma Care Health Syst. 1 (2014) 1000e1119.
[17] D.Y. Lin, Y. Tanaka, M. Iwasaki, A.G. Gittis, H.P. Su, et al., The PD-1/PD-L1 complex resembles the antigen-binding Fv domains of antibodies and T cell receptors, Proc. Natl. Acad. Sci. U. S. A. 105 (2008) 3011–3016.
[18] E. Lazar-Molnar, Q. Yan, E. Cao, U. Ramagopal, S.G. Nathenson, et al., Crystal structure of the complex between programmed death-1 (PD-1) and its ligand PD-L2, Proc. Natl. Acad. Sci. U. S. A. 105 (2008) 10483–10488.
[19] S. Wang, J. Bajorath, D.B. Flies, H. Dong, T. Honjo, et al., Molecular modeling and functional mapping of B7-H1 and B7-DC uncouple costimulatory function from PD-1 interaction, J. Exp. Med. 197 (2003) 1083–1091.
[20] X. Cheng, V. Veverka, A. Radhakrishnan, L.C. Waters, F.W. Muskett, et al., Structure and interactions of the human programmed cell death 1 receptor, J. Biol. Chem. 288 (2013) 11771–11785.
[21] P.A. Kollman, I. Massova, C. Reyes, B. Kuhn, S. Huo, et al., Calculating structures and free energies of complex molecules: combining molecular mechanics and continuum models, Acc. Chem. Res. 33 (2000) 889–897.
[22] B.R. Miller, T.D. McGee, J.M. Swails, N. Homeyer, H. Gohlke, et al., MMPBSA.py: an efficient program for end-state free energy calculations, J. Chem. Theory Comput. 8 (2012) 3314–3321.
[23] H. Sun, Y. Li, S. Tian, L. Xu, T. Hou, Assessing the performance of MM/PBSA and MM/GBSA methods. 4. Accuracies of MM/PBSA and MM/GBSA methodologies evaluated by various simulation protocols using PDBbind data set, Phys. Chem. Chem. Phys. 16 (2014) 16719–16729.
[24] H. Sun, Y. Li, M. Shen, S. Tian, L. Xu, et al., Assessing the performance of MM/PBSA and MM/GBSA methods. 5. Improved docking performance using high solute dielectric constant MM/GBSA and MM/PBSA rescoring, Phys. Chem. Chem. Phys. 16 (2014) 22035–22045.
[25] T. Hou, J. Wang, Y. Li, W. Wang, Assessing the performance of the MM/PBSA and MM/GBSA methods. 1. The accuracy of binding free energy calculations based on molecular dynamics simulations, J. Chem. Inf. Model. 51 (2011) 69–82.
[26] T. Hou, J. Wang, Y. Li, W. Wang, Assessing the performance of the molecular mechanics/Poisson Boltzmann surface area and molecular mechanics/generalized Born surface area methods. II. The accuracy of ranking poses generated from docking, J. Comput. Chem. 32 (2011) 866–877.
[27] J.M. Wang, T. Hou, X. Xu, Recent advances in free energy calculations with a combination of molecular mechanics and continuum models, Curr. Comput.-Aided Drug Des. 2 (2006) 287–306.
[28] L. Xu, H. Sun, Y. Li, J. Wang, T. Hou, Assessing the performance of MM/PBSA and MM/GBSA methods. 3. The impact of force fields and ligand charge models, J. Phys. Chem. B 117 (2013) 8408–8421.
[29] D.E. Friesen, K.H. Barakat, V. Semenchenko, R. Perez-Pineiro, B.W. Fenske, et al., Discovery of small molecule inhibitors that interact with γ-tubulin, Chem. Biol. Drug Des. 79 (2012) 639–652.
[30] J.A. Tuszynski, T.J. Craddock, J.Y. Mane, K. Barakat, C.-Y. Tseng, et al., Modeling the yew tree tubulin and a comparison of its interaction with Paclitaxel to human tubulin, Pharm. Res. 29 (2012) 3007–3021.
[31] K.H. Barakat, M. Houghton, D.L. Tyrrel, J.A. Tuszynski, Rational drug design: one target, many paths to it, Int. J. Comput. Models Algorithms Med. 4 (2014) 59–85.
[32] S.Y. Huang, Search strategies and evaluation in protein–protein docking: principles, advances and challenges, Drug Discov. Today 19 (8) (2014) 1081–1096.
[33] K. Wiehe, B. Pierce, J. Mintseris, W.W. Tong, R. Anderson, et al., ZDOCK and RDOCK performance in CAPRI rounds 3, 4, and 5, Proteins 60 (2005) 207–213.
[34] R. Chen, L. Li, Z. Weng, ZDOCK: an initial-stage protein-docking algorithm, Proteins 52 (2003) 80–87.
[35] M. Ahmed, M.M. Sadek, R.A. Serrya, Kafafy A.-H.N., K.A. Abouzid, et al., Assessment of new anti-HER2 ligands using combined docking, QM/MM scoring and MD simulation, J. Mol. Graphics Modell. 40 (2013) 91–98.
[36] M. Ahmed, M.M. Sadek, K.A. Abouzid, F. Wang, In silico design: extended molecular dynamic simulations of a new series of dually acting inhibitors against EGFR and HER2, J. Mol. Graphics Modell. 44 (2013) 220–231.
[37] M. Ahmed, S. Bird, F. Wang, E. Palombo, In silico investigation of lactone and thiolactone inhibitors in bacterial quorum sensing using molecular modeling, Int. J. Chem. 5 (2012) 49–56.
[38] A. Anwar-Mohamed, K.H. Barakat, R. Bhat, S.Y. Noskov, D.L. Tyrrell, et al., A human ether-a-go-go-related (hERG) ion channel atomistic model generated by long supercomputer molecular dynamics simulations and its use in predicting drug cardiotoxicity, Toxicol. Lett. 230 (2014) 382–392.
[39] M. Gajewski, J. Tuszynski, K. Barakat, J. Huzil, M. Klobukowski, Interactions of laulimalide, peloruside, and their derivatives with the isoforms of β-tubulin, Can. J. Chem. 91 (2013) 511–517.
[40] G. Hu, K. Wang, J. Groenendyk, K. Barakat, M.J. Mizianty, et al., Human structural proteome-wide characterization of Cyclosporine A targets, Bioinformatics 30 (2014) 3561–3566.
[41] K.H. Barakat, J.T. Huzil, K.E. Jordan, C. Evangelinos, M. Houghton, et al., A computational model for overcoming drug resistance using selective dual-inhibitors for aurora kinase A and its T217D variant, Mol. Pharm. 10 (2013) 4572–4589.
[42] J.A. Tuszynski, T.J. Craddock, J.Y. Mane, K. Barakat, C.Y. Tseng, et al., Modeling the yew tree tubulin and a comparison of its interaction with paclitaxel to human tubulin, Pharm. Res. 29 (2012) 3007–3021.
[43] S. Dai, R. Jia, X. Zhang, Q. Fang, L. Huang, The PD-1/PD-Ls pathway and autoimmune diseases, Cell Immunol. 290 (2014) 72–79.
[44] L. Xu, Y. Li, H. Sun, D. Li, T. Hou, Structural basis of the interactions between CXCR4 and CXCL12/SDF-1 revealed by theoretical approaches, Mol. Biosyst. 9 (2013) 2107–2117.
[45] L.P. Jordheim, K.H. Barakat, L. Heinrich-Balard, E.-L. Matera, E. Cros-Perrial, et al., Small molecule inhibitors of ERCC1-XPF protein–protein interaction synergize alkylating agents in cancer cells, Mol. Pharmacol. 84 (2013) 12–24.
[46] K.H. Barakat, M.M. Gajewski, J.A. Tuszynski, DNA polymerase beta (pol beta) inhibitors: a comprehensive overview, Drug Discov. Today 17 (2012) 913–920.
[47] K.H. Barakat, A. Anwar-Mohamed, J.A. Tuszynski, M.J. Robins, D.L. Tyrrell, et al., A refined model of the HCV NS5A protein bound to daclatasvir explains drug-resistant mutations and activity against divergent genotypes, J. Chem. Inf. Model. (2014), http://dx.doi.org/10.1021/ci400631n, http://pubs.acs.org/doi/abs/10.1021/ci400631n
[48] L. Kalé, R. Skeel, M. Bhandarkar, R. Brunner, A. Gursoy, et al., NAMD2: greater scalability for parallel molecular dynamics, J. Comput. Phys. 151 (1999) 283–312.
[49] V. Hornak, R. Abel, A. Okur, B. Strockbine, A. Roitberg, et al., Comparison of multiple Amber force fields and development of improved protein backbone parameters, Proteins 65 (2006) 712–725.
[50] T.J. Dolinsky, P. Czodrowski, H. Li, J.E. Nielsen, J.H. Jensen, et al., PDB2PQR: expanding and upgrading automated preparation of biomolecular structures for molecular simulations, Nucleic Acids Res. 35 (2007) W522–W525.
[51] K. Barakat, J. Tuszynski, Relaxed complex scheme suggests novel inhibitors for the lyase activity of DNA polymerase beta, J. Mol. Graphics Modell. 29 (2011) 702–716.
[52] D.L. Davies, D.W. Bouldin, A cluster separation measure, IEEE Trans. Pattern Anal. Mach. Intell. 1 (1979) 224.
[53] J. Shao, S. Tanner, N. Thompson, T. Cheatham, Clustering molecular dynamics trajectories: 1. Characterizing the performance of different clustering algorithms, J. Chem. Comput. (2007) 2312.
[54] R. Chen, L. Li, Z. Weng, ZDOCK: an initial-stage protein-docking algorithm, Proteins Struct. Funct. Genet. 52 (2003) 80–87.
[55] B.G. Pierce, Y. Hourai, Z. Weng, Accelerating protein docking in ZDOCK using an advanced 3D convolution library, PLoS ONE 6 (2011) e24657.
[56] R. Chen, Z. Weng, Docking unbound proteins using shape complementarity, desolvation, and electrostatics, Proteins Struct. Funct. Genet. 47 (2002) 281–294.
[57] R. Chen, Z. Weng, A novel shape complementarity scoring function for protein–protein docking, Proteins Struct. Funct. Genet. 51 (2003) 397–408.
[58] H.A. Gabb, R.M. Jackson, M.J.E. Sternberg, Modelling protein docking using shape complementarity, electrostatics and biochemical information, J. Mol. Biol. 272 (1997) 106–120.
[59] E. Katchalski-Katzir, I. Shariv, M. Eisenstein, A.A. Friesem, C. Aflalo, et al., Molecular surface recognition: determination of geometric fit between proteins and their ligands by correlation techniques, Proc. Natl. Acad. Sci. U. S. A. 89 (1992) 2195–2199.
[60] K.H. Barakat, J. Law, A. Prunotto, W.C. Magee, D.H. Evans, et al., Detailed computational study of the active site of the hepatitis C viral RNA polymerase to aid novel drug design, J. Chem. Inf. Model. 53 (2013) 3031–3043.
[61] K. Barakat, J. Mane, D. Friesen, J. Tuszynski, Ensemble-based virtual screening reveals dual-inhibitors for the p53-MDM2/MDMX interactions, J. Mol. Graph. Model. 28 (2010) 555–568.
[62] D.E. Friesen, K.H. Barakat, V. Semenchenko, R. Perez-Pineiro, B.W. Fenske, et al., Discovery of small molecule inhibitors that interact with gamma-tubulin, Chem. Biol. Drug Des. 79 (2012) 639–652.
[63] S. Genheden, U. Ryde, How to obtain statistically converged MM/GBSA results, J. Comput. Chem. 31 (2010) 837–846.